

Beating the classical phase precision limit using a quantum neuromorphic platform

Tanjung Krisnanda,¹ Sanjib Ghosh,¹ Tomasz Paterek,² Wiesław Laskowski,^{2,3} and Timothy C. H. Liew^{1,4}

¹*School of Physical and Mathematical Sciences, Nanyang Technological University, 637371 Singapore, Singapore*

²*Institute of Theoretical Physics and Astrophysics, Faculty of Mathematics, Physics and Informatics, University of Gdańsk, 80-308 Gdańsk, Poland*

³*International Centre for Theory of Quantum Technologies, University of Gdańsk, 80-308 Gdańsk, Poland*

⁴*MajuLab, International Joint Research Unit UMI 3654, CNRS, Université Côte d'Azur, Sorbonne Université, National University of Singapore, Nanyang Technological University, Singapore*

Phase measurement constitutes a key task in many fields of science, both in the classical and quantum regime. The higher precision of such measurement offers significant advances, and can also be utilised to achieve finer estimates for quantities such as distance, the gravitational constant, electromagnetic field amplitude, etc. Here we theoretically model the use of a quantum network, composed of a randomly coupled set of two-level systems, as a processing device for phase measurement. An incoming resource state carrying the phase information interacts with the quantum network, whose emission is trained to produce a desired output signal. We demonstrate phase precision scaling following the standard quantum limit, the Heisenberg limit, and beyond. This can be achieved using quantum resource states such as NOON states or other entangled states, however, we also find that classically correlated mixtures of states are alone sufficient, provided that they exhibit quantum coherence. Our proposed setup does not require conditional measurements, and is compatible with many different types of coupling between the quantum network and the phase encoding state, hence making it attractive to a wide range of possible physical implementations.

Keywords: Phase estimation, standard quantum limit, Heisenberg limit, quantum neural network, quantum reservoir processing, quantum metrology.

I. INTRODUCTION

Superior precision in measurements is of great value in ample situations, across many scientific disciplines. For the case of optical phase measurements, conventional methods involve the use of classical light (laser), passing through a material (sample) after which the signal undergoes interference with a reference, resulting in an output containing phase information from the sample. However, this method can be detrimental, especially for sensitive samples with a large number of penetrating photons, which can alter their phase. Furthermore, for samples with fluctuating phases, a method capable of performing rapid phase estimation is desired. In this case, the laser power limits the number of photons emitted per unit time. Consequently the race is towards performing phase estimation with limited number of photons and obtaining high precision output, the regime of which quantum systems offer supremacy over classical counterparts.

In this direction, the classical limitation for the precision of phase ϕ is given by the so-called standard quantum limit (SQL), which lower bounds the error $\Delta\phi$ as in the central limit theorem, i.e., $\Delta\phi \propto 1/\sqrt{N}$, where N is the number of particles used in the measurement. To overcome this, quantum states possessing quantum

properties such as entanglement have been proposed as a resource to obtain precision below the SQL and reach a scaling $\Delta\phi \propto 1/N$, i.e., the so-called Heisenberg limit (HL) [1]. Going beyond the SQL has been demonstrated in a number of experiments, for example: optical phase measurements [2–5]; matter phase [6, 7]; sensing of a single ion mechanical oscillator [8]; and for magnetic field [9–11] as well as electric field sensing [12]. It is also expected to enhance the detection of gravitational waves at the LIGO [13].

A phase estimation setup overcoming the SQL, conventionally involves a Mach-Zehnder interferometer or an improved version [1–7], from which the output retrieves the phase information. One of the forms of resource state known as a NOON state was proven useful, i.e., $(|N0\rangle + |0N\rangle)/\sqrt{2}$, where N denotes the number of excitations. Earlier work utilised these states to demonstrate phase super resolution, corresponding to interference oscillation N times that of single photon resource states [14–16]. Super sensitivity, which is associated with phase precision beating the SQL, was reported for $N = 2$ [4], $N = 4$ [2], and approaching the HL for $N = 3$ [5]. However, following this method, going towards the HL for higher N -NOON states comes with an increasing complexity, requiring conditional measurements.

Recently, neural networks have been fruitful for solving complex problems in a number of fields [17–26]. In general, one has an input, a trained network composed of connected nodes that acts as a processing device, and

Corresponding authors: T.K. (tanjung.krisnanda@ntu.edu.sg) or T.C.H.L. (TimothyLiew@ntu.edu.sg)

an output. Among the different forms of neural network architectures, reservoir computing transpires as one of the competitive candidates [27–36], particularly for direct hardware implementation. Reservoir computing does not require training over the internal connections between network nodes, rather, it is performed only on a single output layer, in which the signals from the network are processed to produce a desired output. The vast progress of this field has also reached the quantum regime – termed quantum reservoir computing or processing. In this case, a quantum network is utilised to execute classical tasks outperforming classical networks [37–40] and also quantum information tasks, such as: state characterisation [41, 42]; preparation of quantum resource states [43, 44]; and a platform for quantum computing [45]. See also Refs. [46, 47] for comparison of different implementations.

Motivated by the direction towards high precision measurements and the vastly growing field of neural networks, here we demonstrate theoretically the use of a quantum network as a processing device for high precision phase measurement. In particular, a resource state carrying phase information after passing through a sample acts as an input, which then interacts with a quantum network (QN) composed of randomly coupled two-level quantum systems, which we refer to as network nodes. The emission from the network (or the measured occupations of the network nodes) is then linearly combined through an output layer, which is trained using ridge regression, in order to generate a desired output signal. We show that our method can perform phase estimation with precision adhering to the SQL, HL, and beyond. We also show that higher QN size offers improved precision and that one can utilise time-integrated measurements for the emission from the QN before combination through an output layer, which is experimentally friendly. We also discuss different types of noise that may affect the QN nodes. Our method is applicable for different types of coupling involved between the input and the network, thus making it desirable for a wide range of physical implementations. Last, we compare our results to the quantum Cramér-Rao bound and show that for some QN parameters, one may obtain near-saturation phase estimation errors.

II. THE SETUP

Here we consider a generic simple model and note that our treatment can potentially be applied to physical systems for experimental realisations, such as: randomly coupled quantum dots [48, 49]; arrays of atomic systems [50–55]; photonic modes in connected optical resonators [56–58] or coupled waveguides [59]; interacting exciton-polariton systems [60–63]; superconducting qubits [64–67]; and programmable QN with a multimode fibre [68].

We define a quantum network as a collection of two-

level quantum systems with random energies and all-to-all couplings as illustrated in Fig. 1. In this paper, we utilise a bipartite (two-mode) state $|\psi_N\rangle$, which, after obtaining a phase information ϕ through the sample, interacts with the network. We take all couplings to be energy-preserving, i.e., Josephson or Jaynes-Cummings type, such that the Hamiltonian is written as

$$\hat{H} = \sum_j^Q E_j \hat{b}_j^\dagger \hat{b}_j + \sum_{jj'}^Q C_{jj'} \left(\hat{b}_j^\dagger \hat{b}_{j'} + \hat{b}_j \hat{b}_{j'}^\dagger \right) + \sum_j^Q \sum_{k=1,2} W_{jk} \left(\hat{a}_k^\dagger \hat{b}_j + \hat{b}_j^\dagger \hat{a}_k \right), \quad (1)$$

where E_j is the energy of the j th node, whose annihilation (creation) operator is denoted by \hat{b}_j (\hat{b}_j^\dagger), $C_{jj'}$ the coupling strengths between the QN nodes, and W_{jk} stands for the coupling strength between the network node j and an input mode k . We have used Q to indicate the number of nodes used in the QN. We also consider other types of coupling, i.e., ultra strong non-energy preserving and cascading type – see Appendix A for detailed expressions.

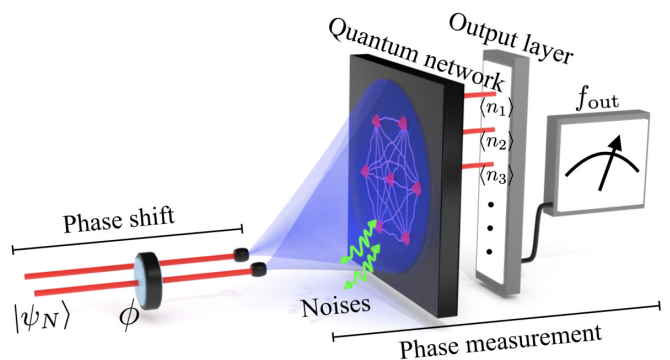


FIG. 1. Setup for high precision phase measurement. A quantum resource state $|\psi_N\rangle$ picks up a phase, after which it interacts with a quantum network consisting of randomly coupled two-level nodes. The phase information is embedded in the QN and retrieved through its emission (estimated mean values after a finite number of repetitions), which is processed via a trained output layer. With this method, we show the phase precision limit following the standard quantum limit, the Heisenberg limit, and beyond.

As the input for the QN, we first consider NOON states, which we write as

$$|\psi_N\rangle \equiv \frac{1}{\sqrt{2}} (|N0\rangle - |0N\rangle), \quad (2)$$

where N denotes the number of excitations. The preparation of NOON states has been demonstrated experimentally, e.g., in Refs. [14, 15, 69]. See also Ref. [44] for their preparation, specifically in the form of Eq. (2). Note that a relative phase in the input state, such as the minus sign in Eq. (2) is irrelevant for the present task. One can utilise other forms of resource state, e.g., we

will also use maximally entangled states and classically correlated states later. After passing one mode of the state through the sample, the state carrying the phase information reads $(|N0\rangle - \exp(iN\phi)|0N\rangle)/\sqrt{2}$.

For the dynamics of our setup, in addition to the coherent evolution corresponding to the Hamiltonian of Eq. (1), we also consider the quantum network being subjected to noises. In particular, we write the evolution of the density matrix ρ of the whole system as follows:

$$\rho(t + \Delta t) = \hat{D}(\Delta t) \hat{U}(\Delta t) [\rho(t)], \quad (3)$$

where \hat{D} and \hat{U} denote the application of possible noise channels and unitary $\exp(-i\hat{H}\Delta t/\hbar)$, respectively. We take into account the energy decay \hat{D}_{dcy} , dephasing \hat{D}_{dph} , and depolarising \hat{D}_{dpl} processes affecting the QN nodes. See Appendix B for explicit expressions, where the strength of the noises is characterised by $\gamma_{\text{dcy}}, \gamma_{\text{dph}}, \gamma_{\text{dpl}}$, in units of energy.

We assume that it is possible to estimate the mean excitation numbers of the QN nodes and that they can be linearly combined with a set of tuneable weights. This corresponds to the action of an output layer of our network, producing an output signal:

$$f_{\text{out}} = \alpha_0 + \alpha_1 \langle n_1 \rangle + \alpha_2 \langle n_2 \rangle + \dots + \alpha_Q \langle n_Q \rangle, \quad (4)$$

where $\langle n_j \rangle = \text{tr}(\hat{b}_j^\dagger \hat{b}_j \rho(\tau))$ denotes the ideal mean excitation of the j th QN node at time τ . The coefficients, written in a vector form, $\boldsymbol{\alpha} \equiv (\alpha_0, \alpha_1, \alpha_2, \dots, \alpha_Q)^T$ are trained such that the error of the output signal is minimised. The training is performed with ridge regression (see Appendix C for details). Later, we show that our method also allows for time-integrated measurements (instead of time-resolved at time τ), i.e., $f_{\text{out}} = \alpha_0 + \alpha_1 \int \langle n_1 \rangle dt/T + \alpha_2 \int \langle n_2 \rangle dt/T + \dots$, where T is the measurement duration.

In experimental situations, mean excitation numbers are determined from a finite number of measurements and their optimal use is the subject of metrology. To account for the deviation from the ideal values, which require an infinite number of measurements, we introduce a random error as follows

$$\langle n_j \rangle = \langle n_j \rangle_{\text{ideal}} + \varepsilon_j, \quad (5)$$

where $\langle n_j \rangle_{\text{ideal}} = \text{tr}(\hat{b}_j^\dagger \hat{b}_j \rho(\tau))$ and ε_j is a random number normally distributed with zero mean and standard deviation of the mean (SDM) $\xi/2$. By the central limit theorem it follows that $\xi \propto 1/\sqrt{M}$ (the SQL), where M is the number of measurements. We note that for $\xi \rightarrow 0$, the simulations show that our method reproduces $\Delta\phi \rightarrow 0$ for phase estimation as it should be since this corresponds to $M \rightarrow \infty$. Importantly, the addition of systematic errors in Eq. (5) has no effect on $\Delta\phi$, because the training procedure learns to overcome them.

III. RESULTS

In what follows, we shall set the network parameters $(E_j, C_{jj'}, W_{jk}) = (e_j, c_{jj'}, w_{jk})\hbar\Omega$, where the lowercase parameters are dimensionless and $\hbar\Omega$ has units of energy. To simulate the imperfections in fabrication of the QN, we generate random parameters $(e_j, c_{jj'}, w_{jk}) \in [0, 1]$ that are uniformly distributed. As the initial condition for the QN, we assume the experimentally sensible ground state for all the nodes, i.e., $|0\rangle^{\otimes Q}$.

A. Output signal

Following the discussion from Refs. [1, 2], we take the following function as the target output signal:

$$I_{\text{ideal}} = \frac{1}{2} (1 - \cos(N\phi)), \quad (6)$$

where N corresponds to the degree of NOON states used in the input. The function I_{ideal} can show both super resolution due to its $N\phi$ dependence and super sensitivity, which we will demonstrate later. For one realisation of the set of random network parameters $(e_j, c_{jj'}, w_{jk})$, the assessment of our method is conducted as follows. For the training procedure, we generate N_{train} random phases ϕ , which lead to N_{train} sets of $(\langle n_1 \rangle, \langle n_2 \rangle, \dots, \langle n_Q \rangle)$ from the realised QN, and in each set the mean values are estimated after M measurements according to Eq. (5). The coefficients $\boldsymbol{\alpha}$ (output layer) are trained using the N_{train} training sets with ridge regression (see Appendix C) such that the estimated output signal,

$$I_{\text{est}} = \alpha_0 + \alpha_1 \langle n_1 \rangle + \alpha_2 \langle n_2 \rangle + \dots + \alpha_Q \langle n_Q \rangle, \quad (7)$$

is close to the ideal form in Eq. (6). To test the trained output layer, we generate N_{test} random phases, labelled ϕ_l , which consequently give an estimated output signal $I_{\text{est},l}$. We note that the training is performed only once, after which we obtain the coefficients $\boldsymbol{\alpha}$ that one can use to retrieve the estimated output of any phase ϕ_l .

We present in Fig. 2, an exemplary demonstration of our method using one realisation of the network parameters, showing estimated output signals (filled circles) and the corresponding ideal ones (solid curves). We utilised NOON states $N = 1, 2, 3$, and 4. In all cases, we used $N_{\text{train}} = 10$ and $N_{\text{test}} = 50$, the measurement error $\xi = 0.01$, and a quantum network of size 4 with evolution time $\tau = 8/\Omega$. Fig. 2 shows super resolution for higher N -NOON states, as seen from the $2\pi/N$ period of oscillations in the range $\phi \in [0, 2\pi)$. It is also intuitive that the retrieval of the phase ϕ_{est} from I_{est} has different accuracy for different ϕ . In particular, the accuracy is best in the region of highest slope, e.g., $\phi = \pi/2N$ for the case of N -NOON state. This will be quantified and demonstrated in more detail in the next section.

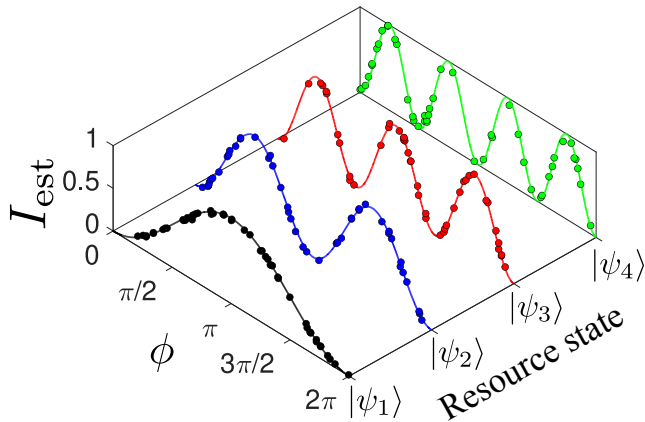


FIG. 2. Exemplary output signals showing super resolution. Different NOON states $|\psi_N\rangle$ were used as input for a quantum network of size 4. The corresponding solid curves indicate the ideal signals I_{ideal} . In all cases, the training and testing size is 10 and 50, respectively, with $\xi = 0.01$.

B. Phase estimation

We evaluate the phase from the output signal (for N -NOON state) as

$$\phi_{\text{est}} = \frac{1}{N} \arccos(1 - 2I_{\text{est}}). \quad (8)$$

The measurement error ε_j in Eq. (5) can result in an output signal $I_{\text{est}} \notin [0, 1]$ at extreme regions, e.g., $\phi \approx 0$ and π/N in Fig. 2, which further gives a complex ϕ_{est} . To avoid these instances, we assign $\phi_{\text{est}} = 0$ and $\phi_{\text{est}} = \pi/N$, for $I_{\text{est}} < 0$ and $I_{\text{est}} > 1$, respectively. The error for the phase estimation task is quantified as follows:

$$\Delta\bar{\phi}_N = \sqrt{\sum_l^{N_{\text{test}}} \frac{(\phi_{\text{est},l} - \phi_l)^2}{N_{\text{test}}(N_{\text{test}} - 1)}}. \quad (9)$$

Note that the bar notation indicates the testing is performed, where the phases ϕ_l are randomly generated over a range of values, e.g., $[0, \pi/N]$. For a particular value of the testing phase, i.e., $\phi_l = \text{constant}$, the above expression reduces to the SDM of that phase, which we shall write simply as $\Delta\phi_N$ hereafter.

We demonstrate the estimated phase vs ideal phase in Fig. 3 for different strengths of the measurement error: $\xi = 10^{-2}$ (a), 5×10^{-3} (b), and 10^{-3} (c). We have used a quantum network with 4 nodes that is evolved for $\tau = 8/\Omega$, NOON state $|\psi_1\rangle$ as the input resource state, 10 training sets, and 100 testing sets. It can be seen that ϕ_{est} deviates more from the ideal phase near $\phi = 0$ and π (low output slope, see Fig. 2), while showing best accuracy at $\phi = \pi/2$. It is also clear that smaller measurement error ξ produces less error in the estimated phase.

Fig. 3(d) compares the performance of different QN sizes, i.e., $Q = 2$ (squares), 3 (triangles), and 4 (circles)

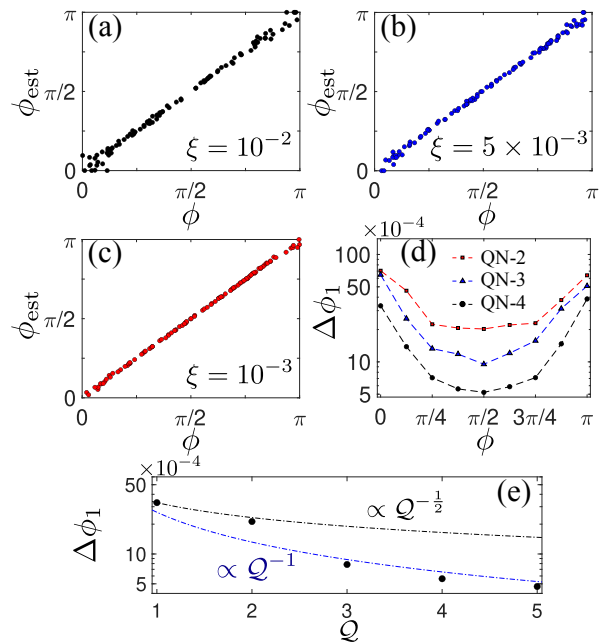


FIG. 3. Performance of phase estimation task. (a)-(c) Estimated phase vs ideal phase for different measurement error ξ , indicated on the bottom right of each panel. A QN with 4 nodes was used in these simulations. (d) SDM at different ϕ for different network sizes: (2, 3, 4) indicated by (squares, triangles, circles), respectively, and $\xi = 10^{-3}$. (e) $\Delta\phi_1$ at $\pi/2$ indicating the scaling with QN size. Each SDM is averaged over 50 sets of realisations of the random network parameters. In all considered cases, for each realisation of the network parameters, $|\psi_1\rangle$ was used with 10 training and 100 testing sets.

with $\tau = 8/\Omega$. NOON state $|\psi_1\rangle$ and a measurement error $\xi = 10^{-3}$ were used in all three cases. We realised 50 sets of the random network parameters, in each of which we used $N_{\text{train}} = 10$ and $N_{\text{test}} = 100$. We computed the SDM $\Delta\phi_1$ (averaged over 50 sets of QN realisation) at different ϕ . This way, our method is not highly dependent on a particular realisation of the network parameters. It is clear that more network nodes produce less error. Moreover, Fig. 3(d) not only indicates that the least error is found around $\phi = \pi/2$, but also how the error behaves as a function of ϕ . Additionally, Fig. 3(e) shows how the phase estimation error $\Delta\phi_1$ changes with respect to the QN size Q . The scaling exceeds $\propto Q^{-1/2}$, which is the SQL with respect to the number of QN nodes.

For any to-be-measured phase ϕ , one can train the QN with a “shift”, i.e., $I_{\text{ideal}} = (1 - \cos(N(\phi + \theta)))/2$. The shift θ is chosen such that the highest output slope is located around ϕ , resulting in the minimum SDM of the phase. See a demonstration in Appendix D. Hereafter, the SDM $\Delta\phi_N$ for any random ϕ will be assumed at the highest output slope. Note that this procedure is all done in the data processing step (post measurements). The next section quantifies and expands on the observations made about Fig. 3.

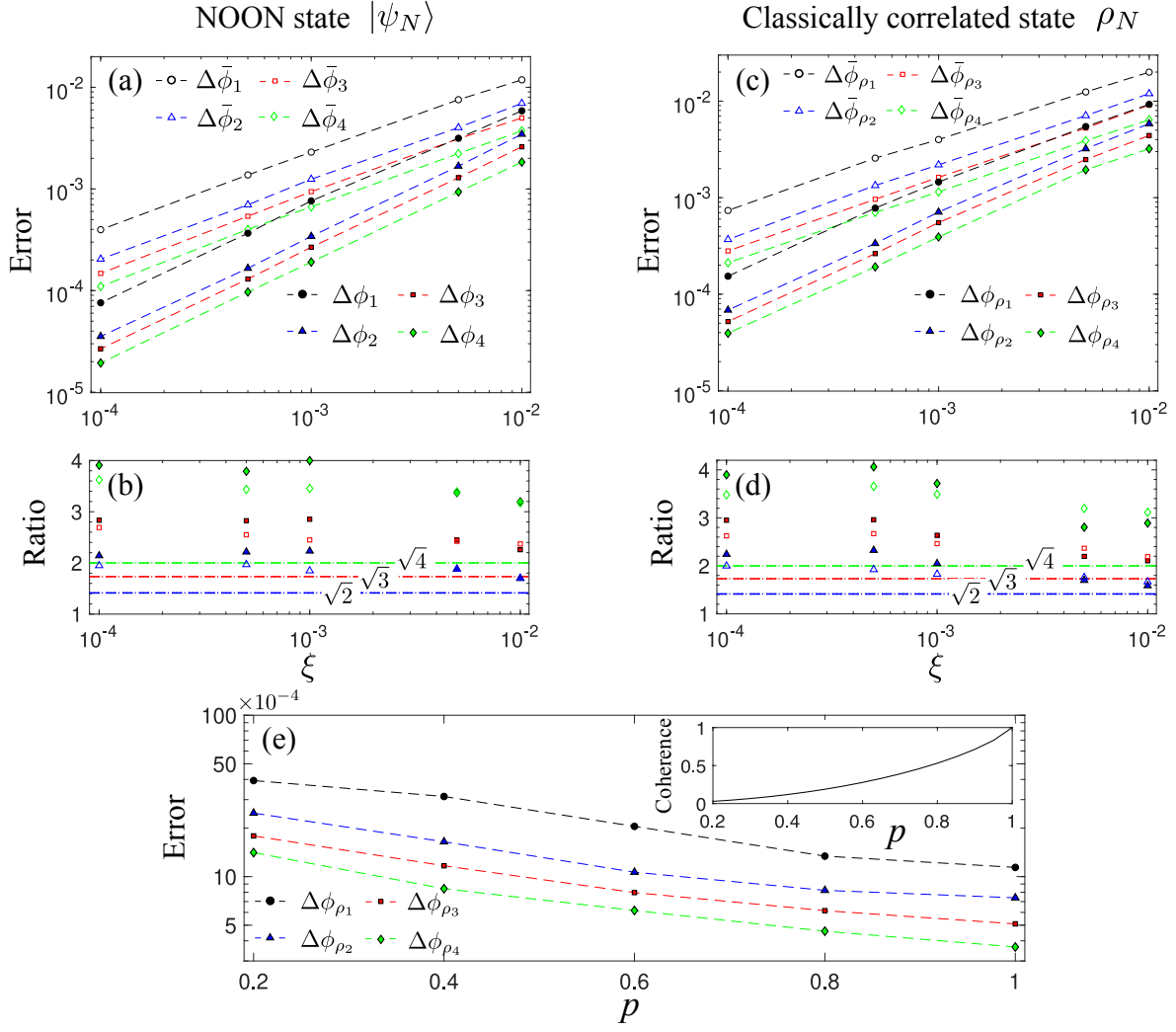


FIG. 4. Phase precision showing the standard quantum limit and Heisenberg limit. (a) Phase estimation errors $\Delta\bar{\phi}_N$ and the SDM at highest output slope $\Delta\phi_N$, plotted against the measurement error ξ ($\propto 1/\sqrt{M}$). We have used N to denote the use of N -NOON state. (b) The ratio of phase estimation errors, see Eq. (10). Empty triangles are for $\bar{\eta}_{12}$, empty squares for $\bar{\eta}_{13}$, and empty diamonds for $\bar{\eta}_{14}$. Also the corresponding filled ones: η_{12} (triangles), η_{13} (squares), and η_{14} (diamonds). We report that $\Delta\bar{\phi}_N, \Delta\phi_N \propto 1/\sqrt{M}$ – demonstrating the SQL limit, and $\Delta\bar{\phi}_N, \Delta\phi_N \propto 1/N$ – demonstrating the HL limit. Panels (c) and (d) are the phase estimation errors and their ratios, respectively, using the classically correlated state ρ_N in Eq. (11). (e) Estimation errors using ρ_N dephased in the Fock basis, modelled by multiplying the off-diagonal elements of ρ_N with a positive coefficient $p \leq 1$. The inset shows the amount of coherence in the state ρ_N with respect to p . In all cases, each data point represents an error evaluation of a trained output layer with 10 training and 100 testing sets, which is averaged over 50 different realisations of network parameters.

C. Phase precision scaling

Here we demonstrate phase precision scaling, which follows the SQL, and HL by utilising higher degree N -NOON states. For this purpose, we used a QN composed of 4 nodes, evolved for $\tau = 12/\Omega$. Fig. 4(a) presents the phase estimation errors, both $\Delta\bar{\phi}_N$ and the SDM $\Delta\phi_N$ at the highest output slope, where N indicates the use of N -NOON state. These errors were plotted against the measurement error ξ , defined in Eq. (5). We generated 50 different sets of realisations of the network parameters. In each of these sets, we performed the training of the

output layer with $N_{\text{train}} = 10$ and the phase estimation error was tested with $N_{\text{test}} = 100$. Each data point in Fig. 4(a) is the average phase estimation error of the 50 different realisations. One can see that $\Delta\bar{\phi}_N, \Delta\phi_N \propto \xi$. As $\xi \propto 1/\sqrt{M}$, where M denotes the number of measurements, it follows that $\Delta\bar{\phi}_N, \Delta\phi_N \propto 1/\sqrt{M}$, which is the SQL statement.

We now evaluate closer the use of higher N -NOON states for a better scaling option. The argument goes as follows: for example, instead of having double the number of measurements with $|\psi_1\rangle$ one can utilise $|\psi_2\rangle$, and harness the quantum advantage for precision beyond

the SQL. Note that the comparison is made, where in both cases, one has the same number of photons passing through the sample. For a more general scenario, in order to beat the SQL, one has to show that the phase error for N -NOON state ($N > 1$) gives a ratio

$$\bar{\eta}_{1N} \equiv \Delta\bar{\phi}_1/\Delta\bar{\phi}_N > \sqrt{N}, \quad (10)$$

or for the case of SDM, $\eta_{1N} \equiv \Delta\phi_1/\Delta\phi_N > \sqrt{N}$. Fig. 4(b) shows the ratio $\bar{\eta}_{1N}$: empty triangles ($N = 2$), squares (3), and diamonds (4), and the corresponding filled ones for η_{1N} . Indeed, not only the ratios exceed the SQL scaling indicated by the dash-dotted lines, they also approach $\bar{\eta}_{1N}, \eta_{1N} \rightarrow N$ – the HL scaling.

The quantum network platform allows for precision beyond the SQL even if the input resource states do not possess quantum correlations. In this case, we consider states of the form

$$\rho_N = \frac{1}{2}|\psi_N\rangle\langle\psi_N| + \frac{1}{2}|\tilde{\psi}_N\rangle\langle\tilde{\psi}_N| \quad (11)$$

$$= \frac{1}{2}|+-\rangle\langle+-| + \frac{1}{2}|-+\rangle\langle-+|, \quad (12)$$

where we introduced two-mode state $|\tilde{\psi}_N\rangle \equiv (|00\rangle - |NN\rangle)/\sqrt{2}$ and single-mode states $|\pm\rangle = (|0\rangle \pm |N\rangle)/\sqrt{2}$. In order to understand the resources present in ρ_N , let us recall that quantum entanglement is a special type of quantum correlation present between quantum systems [70], and can be quantified, e.g., with negativity [71]. A broader class of quantum correlations is known as quantum discord [72, 73]. It draws the border between quantum and classical correlations, and has been shown as a necessary ingredient for entanglement gain between mediated systems [74–77]. One can infer that not only the state ρ_N is separable (not entangled) $E_{1:2} = 0$, it also has zero quantum discord $D_{1|2} = D_{2|1} = 0$, and hence, contains only classical correlations. This is apparent (without calculations) since ρ_N can be written in a form that only requires orthogonal states for the subsystems, i.e., the $|\pm\rangle$ in Eq. (12). However, it has coherence (off-diagonal elements) when represented in the Fock basis. Also, note that the state ρ_N can be thought of as embedded in a two qubit space, with the levels given by $|0\rangle$ and $|N\rangle$. This way, ρ_N is simply an equal mixture of two Bell-like states.

With the state ρ_N , we performed phase estimation tasks, similar to those in Fig. 4(a). The results are plotted in Fig. 4(c), where the parameters and notation are the same as in Fig. 4(a). Although the phase estimation errors are slightly higher than those in Fig. 4(a), the scaling for higher N still beats the SQL and approaches the HL, see Fig. 4(d). This finding opens up a new path of performing super sensitive phase measurements using resource states that do not have quantum correlations and are relatively easier to prepare. We note that previous work conjectured the role of quantum discord in mixed state quantum metrology [78]. Our work extends this direction and presents metrology without quantum discord. In this case, the coherence of the state ρ_N plays

an important role. In order to demonstrate this more closely, suppose the off-diagonal elements of the state ρ_N are multiplied by a positive number $p \leq 1$, which simulates dephasing in the Fock basis. Complete dephasing is given when $p = 0$, in which case the state, now completely diagonal, cannot carry the phase information ϕ . Phase estimation errors for different values of p are plotted in Fig. 4(e). The inset shows how the coherence, quantified as $S_n(\rho_N(p=0)) - S_n(\rho_N(p))$ [79], where $S_n(\rho) \equiv -\text{tr}(\rho \ln \rho)$ denotes the von Neumann entropy, changes with respect to the variable p . It is clear that states with larger coherence result in less phase estimation errors.

D. Time-resolved and time-integrated processing

Thus far, we have considered processing mean values $\{\langle n_j \rangle\}$ at a particular time τ . One might ask how the quantum advantage (beating the SQL) changes with respect to time. To answer this question, we present the SDM ratio η_{1N} at different times in Fig. 5, both using $Q = 2$ (a) and 4 (b) network nodes. In both panels, the ratios are denoted as: η_{12} (triangles), η_{13} (squares), and η_{14} (diamonds). The corresponding SQL scaling thresholds are indicated by the dash-dotted lines: blue ($\sqrt{2}$), red ($\sqrt{3}$), and green ($\sqrt{4}$). All the values η_{1N} are obtained in the same way as in Fig. 4 for $\xi = 10^{-3}$, i.e., with training size 10, testing size 100, and averaged over 50 realisations of the network parameters. It can be seen that it takes time for the quantum advantage to surface, especially for the case of QN-4, which involves more network nodes. This is intuitive since it requires time for the information to be embedded in the quantum network, even so in one with a bigger size. From Fig. 5, the quantum advantage can reach higher values for QN-2 in the considered time span. However, this does not mean that QN-2 performs better than QN-4, as the bigger size QN offers lower phase estimation errors $\Delta\phi_N$ (not shown). We note that at some times, the quantum advantage exceeds even the HL scaling, e.g., at $\Omega t = 8$ in Fig. 5(a). This is inline with the prediction that interacting systems with multipartite couplings, as it is the case for the QN here, can indeed go beyond the HL [80–82]. We also performed similar analysis using different coupling types and other entangled states as input, see Section III F.

A more experimentally friendly option considers processing time-integrated mean values from the QN nodes to form the estimated output signal, i.e., $I_{\text{est}} = \alpha_0 + \alpha_1 \int \langle n_1 \rangle dt/T + \alpha_2 \int \langle n_2 \rangle dt/T + \dots$, from which the estimated phase ϕ_{est} is calculated. To exemplify this point, we utilised the time-integrated mean values for the scenario in Fig. 5, where the measurement was conducted from $\Omega t = 10.75$ to 11.25. For the case of QN-2 the resulting ratios are $\eta_{12} \approx 2.1$, $\eta_{13} \approx 3.7$, and $\eta_{14} \approx 4.1$, whereas for QN-4 they are given by 2.6, 3.2, and 3.5, respectively. In all cases, the quantum network approach offers quantum advantage, i.e., the ratio beyond the SQL,

and often beyond HL.

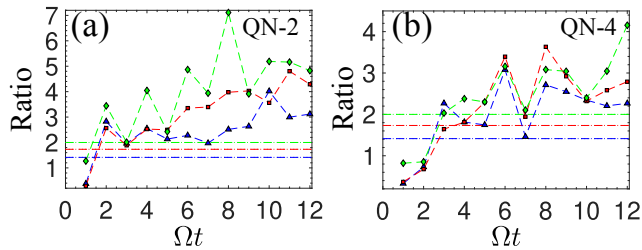


FIG. 5. SDM ratio η_{1N} at different times for quantum network with 2 (a) and 4 (b) nodes. Notation as in Fig. 4(b). At some times, the ratio η_{1N} exceeds not only the SQL (\sqrt{N}) but also the HL (N). Although the ratio at some times for QN-2 is higher, the QN-4 produces less phase estimation errors because its performance for single-excitation NOON state (the reference for the ratio) is much better, see Fig. 3(d).

E. Noises

Here we shall investigate the role of noise, i.e., energy decay, dephasing, and depolarising channels affecting the QN nodes. Let us consider QN-4, where the bigger network size is likely to cause more disturbance from noise, which is evolved for a time $\tau = 6/\Omega$. To scrutinise each source of noise, we shall study the application of the noise channels: energy decay \hat{D}_{dcy} , dephasing \hat{D}_{dph} , and depolarising \hat{D}_{dpl} separately. The strength of these channels are characterised, respectively, by γ_{dcy} , γ_{dph} , and γ_{dpl} in units of energy (see Appendix B for details). For simplicity, we have assumed the same noise strength for all the QN nodes.

In Fig. 6(a) we present the average SDM $\Delta\phi_N$ against the noise-to-QN energy ratio $\gamma/\hbar\Omega$. The filled (empty) symbols indicate the use of $|\psi_1\rangle$ ($|\psi_2\rangle$), with the shapes corresponding to the application of energy decay (circles), dephasing (triangles), and depolarising channel (squares). Similar to the scenario in Fig. 5(b), the average is taken over 50 different realisations of the network parameters, each with 10 training and 100 testing sets. It is apparent that the use of higher N -NOON state, $|\psi_2\rangle$ in Fig. 6(a), is affected more severely by all the noises. This is expected as higher degree NOON states possess more excitations. We also note that depolarising noise has the worst effect on the phase estimation error. This channel corresponds to mixing the state of the QN nodes with a maximally mixed state, rendering part of the network “capacity” useless for information embedding. Note that up to $\gamma/\hbar\Omega = 10^{-2}$, the effects from all the noises are minute. The error ratio η_{12} is plotted in Fig. 6(b) where the affecting noise is energy decay (circles), dephasing (triangles), and depolarising (squares). It can be seen that even in the situation where $\gamma/\hbar\Omega = 0.1$, the quantum advantage still persists.

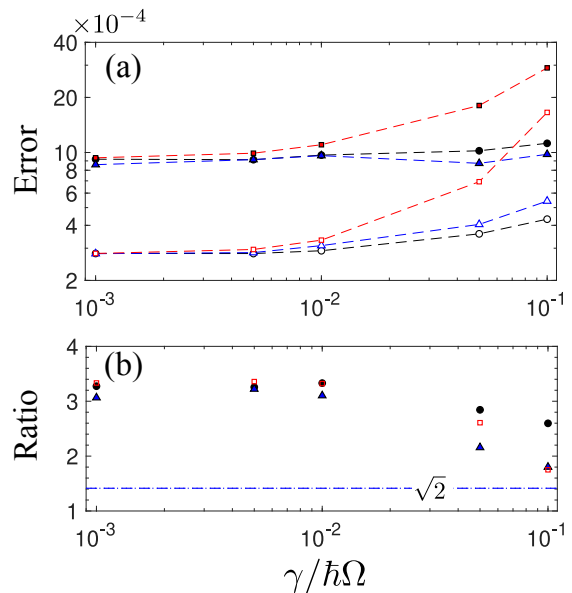


FIG. 6. (a) SDM of highest slope $\Delta\phi_1$ (filled symbols) and $\Delta\phi_2$ (empty symbols) in the presence of energy decay (circles), dephasing (triangles), and depolarising (squares) noise. The axis $\gamma/\hbar\Omega$ refers to the ratio of the strength of respective noise to the energy unit of the quantum network parameters. The simulations were conducted averaging over 50 realisations of network parameters, with 10 training and 100 testing sets. A QN with size 4 was used, and $\tau = 6/\Omega$. (b) The ratio η_{12} of the SDMs in panel (a) for the case of energy decay (circles), dephasing (triangles), and depolarising (squares) noise. Quantum advantage is present for all these noise strengths.

F. Beating SQL with other coupling mechanisms and resource states

Now we demonstrate that our method is not limited to the type of coupling involved between the quantum systems. We shall vary the coupling type between the input and QN nodes, which is responsible for embedding the phase information into the QN. In particular, we consider: energy-preserving type coupling (EP), also known as Jaynes-Cummings or Josephson coupling; ultra strong coupling; and cascading [83, 84] of the input into the QN. The model for ultra strong coupling is similar to the EP, where the last term in the Hamiltonian of Eq. (1) changes to $\sum_j^{\mathcal{Q}} \sum_{k=1,2} W_{jk} \left(\hat{a}_k^\dagger \hat{b}_j + \hat{b}_j^\dagger \hat{a}_k + \hat{a}_k \hat{b}_j + \hat{b}_j^\dagger \hat{a}_k^\dagger \right)$. The addition of the last two terms in the summation indicates strong coherent interactions allowing for simultaneous annihilation and creation of excitations in the input party k and QN node j . For the cascading formalism, see Appendix A for details. Similarly, it involves an input-network coupling coefficient W_{jk} in energy unit. Also, in this formalism the input k experiences an energy decay characterised by a coefficient $\sum_j W_{jk}^2/\gamma$, where γ denotes a constant decay strength for the QN nodes.

Fig. 7 shows the comparison between the EP (a), ultra strong (b), and cascading (c) coupling. In all cases

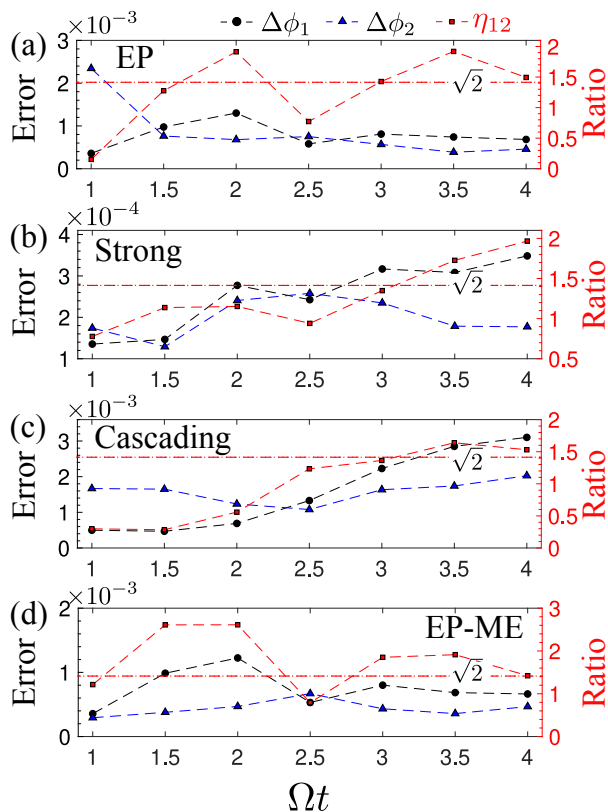


FIG. 7. Comparison of different input-network coupling mechanisms and resource states. (a) Energy-preserving coupling (Jaynes-Cummings or Josephson). (b) Ultra strong coherent interactions (note different vertical scale). (c) Cascading of input into QN nodes. (d) Energy-preserving coupling with maximally entangled states as the input. In all the panels, SDMs $\Delta\phi_1$ and $\Delta\phi_2$ are plotted for different evolution times. The right axis indicates the ratio $\eta_{12} = \Delta\phi_1/\Delta\phi_2$. All the considered cases are capable of beating the SQL threshold (red dash-dotted lines).

we used a QN with size 3, measurement error $\xi = 10^{-3}$, and 50 realisations of the network parameters. At each time Ωt , we performed the training with 10 sets and the testing with 100 sets. For Fig. 7(c) we set the decay $\gamma = \hbar\Omega$. It is worth noting that the ultra strong type coupling produces lesser errors. This is partly because the ultra strong interactions allow for faster information embedding, i.e., the information spreads and occupies the capacity or Hilbert space of the QN more (with the addition of the terms $\hat{a}_k\hat{b}_j + \hat{b}_j^\dagger\hat{a}_k^\dagger$). The cascading coupling has an advantage that the phase information travels in one way (into the QN), unlike the EP and the ultra strong couplings considered in Fig. 7 where the evolution is coherent and part of the information travels back and forth between the input and the QN. Note that with a decay coefficient $\gamma = \hbar\Omega$, the cascading coupling is capable of producing nonclassical precision with estimated errors in the order $\sim 10^{-3}$.

Finally, the results in Fig. 7(d) were obtained with energy-preserving coupling where we used maximally en-

tangled states as the resource (EP-ME). In this case, $|\psi_1\rangle = (|10\rangle + |01\rangle)/\sqrt{2}$ and $|\psi_2\rangle = (|20\rangle + |11\rangle + |02\rangle)/\sqrt{3}$. For the latter, after passing the sample, the input state reads $(|20\rangle + \exp(i\phi)|11\rangle + \exp(i2\phi)|02\rangle)/\sqrt{3}$. This state still carries 2ϕ dependence, and the QN processing produces precision beating the SQL. We note that for EP-ME in Fig. 7(d), we used a slightly modified output model, i.e., $I_{\text{est}} = \alpha_0 + \alpha_1\langle n_1\rangle + \alpha_2\langle n_2\rangle + \alpha_3\langle n_3\rangle + \alpha_4\langle n_1\rangle\langle n_2\rangle + \alpha_5\langle n_2\rangle\langle n_3\rangle + \alpha_6\langle n_3\rangle\langle n_1\rangle + \alpha_7\langle n_1\rangle\langle n_2\rangle\langle n_3\rangle$, where the coefficients were trained with ridge regression. This way, it does not require extra measurements (i.e., only the mean values $\{\langle n_j\rangle\}$, as used in Eq. (7)). We note that in all panels of Fig. 7, the ratio η_{12} exceeds the SQL threshold given by the red dash-dotted lines.

G. The quantum Cramér-Rao bound

In quantum metrology, the minimum phase measurement error follows the so-called quantum Cramér-Rao (QCR) bound:

$$\delta\phi \geq \frac{1}{\sqrt{MF_q(\rho)}}, \quad (13)$$

where M is the number of repetitions (measurements) and $F_q(\rho)$ is the quantum Fisher information (QFI) of a quantum state ρ . Note that $\delta\phi$ is the standard deviation of the measurement error, different from that of Eq. (9) by $\sqrt{N_{\text{test}}}$. The QFI of a general state ρ can be evaluated following the expression given in Refs. [85, 86]. In the present case, we have $F_q(|\psi_N\rangle\langle\psi_N|) = F_q(\rho_N) = N^2$, which gives the QCR bound: $\delta\phi \geq 1/(\sqrt{MN})$.

To compare our scheme to the QCR bound, we slightly modify the model for the measurement of the QN emission, previously described in Eq. (5), to explicitly take into account the number of repetitions M . Given the ideal mean excitation of the j th QN node $\langle n_j \rangle_{\text{ideal}}$, M random numbers are generated, labelled $\mu_m \in [0, 1]$. New values (0 or 1) are assigned as follows: (i) $\tilde{\mu}_m = 0$ if $\mu_m \geq \langle n_j \rangle_{\text{ideal}}$ and (ii) $\tilde{\mu}_m = 1$ if $\mu_m < \langle n_j \rangle_{\text{ideal}}$. This way, $\tilde{\mu}_m$ s mimic real experimental data, the average of which converges to $\langle n_j \rangle_{\text{ideal}}$, with a standard deviation of the mean $\propto 1/\sqrt{M}$.

The phase measurement errors (standard deviation) are plotted in Fig. 8. The resource states in panels (a) and (b) are NOON states $|\psi_N\rangle$, whereas those in panels (c) and (d) are mixed states ρ_N . The performance is plotted against the degree of resource state N in panels (a) and (c), as well as against the number of QN nodes \mathcal{Q} in panels (b) and (d). The QCR bound with $M = 10^4$ is plotted as a dashed-dotted curve or line in all the panels. It can be seen that the minimum standard deviation $\delta\phi_{\text{min}}$ is close to the QCR bound, which indicates that there exists a set of QN parameters allowing for near-saturation performance. This way, one can think of the QN as a measuring and processing device to efficiently extract information from the phase-encoded input state. In principle, one may perform a more rigorous

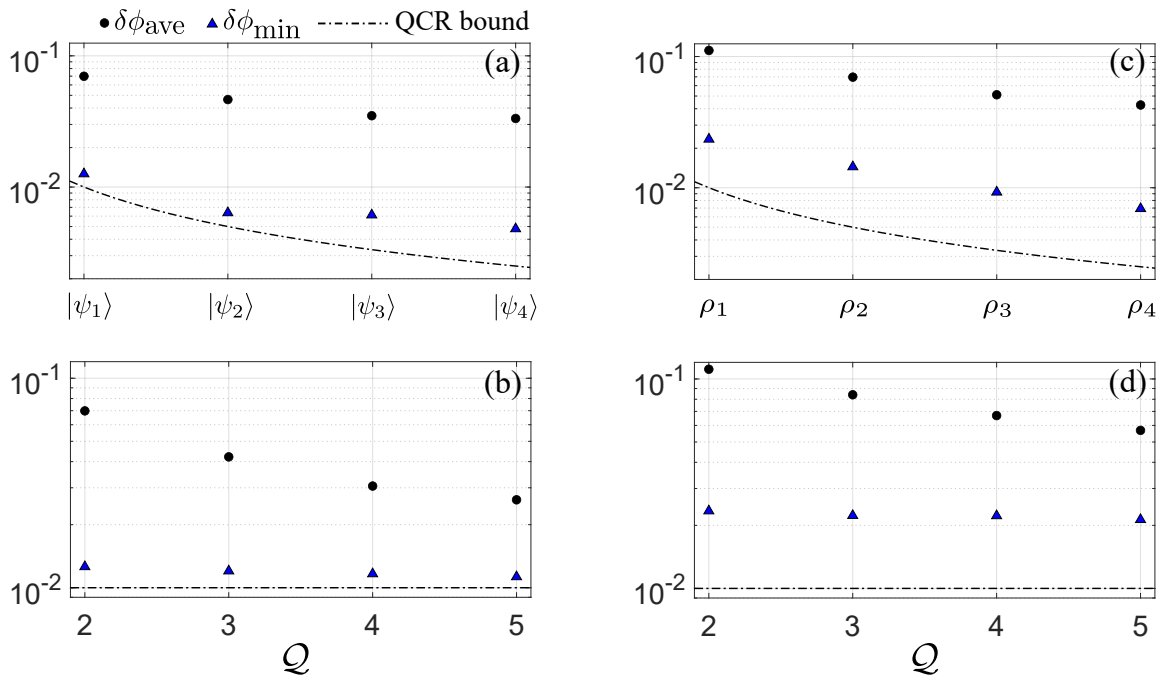


FIG. 8. Comparison of the phase measurement errors using a quantum neuromorphic platform to the quantum Cramér-Rao bound. With respect to 10^3 realisations of the quantum network parameters, the average and minimum phase measurement errors are denoted by the black circles and blue triangles, respectively. The errors are plotted against: (a) different NOON states $|\psi_N\rangle$ using QN of size $Q = 2$; (b) QN sizes using $|\psi_1\rangle$; (c) different mixed states ρ_N using QN of size 2; and (d) different QN sizes using ρ_1 . In all panels, the quantum Cramér-Rao bound is indicated by the black dashed-dotted curve or line, where the number of repetitions is $M = 10^4$. The testing was performed at the highest output slope.

and precise parameter search algorithm to find a better set of parameters for even smaller $\delta\phi_{\min}$. Here we simply take 10^3 random realisations of the QN parameters, with evolution time $\tau = 12/\Omega$. It is expected that the performance of NOON states is better than the mixed states, despite having the same QFI. Here, the scheme might benefit from a more complex QN architecture or a proper parameter search algorithm. We also note that both $\delta\phi_{\text{ave}}$ and $\delta\phi_{\min}$ are better for higher degree N of the resource states and number of QN nodes Q .

IV. CONCLUSION

We have presented a platform for phase estimation tasks, based on a quantum network approach. It consists of three main elements: (1) a resource state carrying a phase information as input; (2) a quantum network, which is made of a collection of randomly connected quantum systems (the nodes), acting as a quantum processing device; and (3) an output layer, which combines the emission or measurement results from the network nodes, and produces the final output. The training is performed in the output layer with ridge regression such that the error of the target output is minimised. The reported precision scales better than the standard quantum limit, and even the Heisenberg limit – owing to the interacting nature of the quantum network. We

have shown that this is possible even with classically correlated states as input owing to quantum coherence.

Our proposed platform is versatile, i.e., it is applicable for different types of coupling between the input and quantum network: the explicit calculations covered Jaynes-Cummings or Josephson; ultra strong; and cascading coupling. It also allows for both time-resolved and time-integrated processing of the network emissions. We show that the resulting quantum advantage is robust against energy decay, dephasing, and depolarising noises. One can further explore other forms of resource states as input or other types of coupling between the quantum systems involved. This makes our platform attractive for a wide range of physical implementations.

ACKNOWLEDGMENT

T.K., S.G., and T.C.H.L. acknowledge the support by the Singapore Ministry of Education under its AcRF Tier 2 grant MOE2019-T2-1-004. T.P. is supported by the Polish National Agency for Academic Exchange NAWA Project No. PPN/PPO/2018/1/00007/U/00001.

Appendix A: Other types of input-network coupling

For ultra strong coupling between the input parties and the quantum network nodes, the evolution is written as in Eq. (3) in the main text where the input-network coupling term in the Hamiltonian of Eq. (1) now reads

$$\sum_j \sum_{k=1,2}^{\mathcal{Q}} W_{jk} \left(\hat{a}_k^\dagger \hat{b}_j + \hat{b}_j^\dagger \hat{a}_k + \hat{a}_k \hat{b}_j + \hat{b}_j \hat{a}_k^\dagger \right).$$

The ultra strong coupling allows for simultaneous annihilation and creation of excitations, i.e., the terms $\hat{a}_k \hat{b}_j + \hat{b}_j^\dagger \hat{a}_k^\dagger$.

We also consider an input-network coupling following the cascading formalism [83, 84]. The Hamiltonian in this case reads

$$\hat{H} = \sum_j^{\mathcal{Q}} E_j \hat{b}_j^\dagger \hat{b}_j + \sum_{jj'}^{\mathcal{Q}} C_{jj'} \left(\hat{b}_j^\dagger \hat{b}_{j'} + \hat{b}_j \hat{b}_{j'}^\dagger \right), \quad (\text{A1})$$

and the cascading master equation has the following structure:

$$\begin{aligned} \rho(t + \Delta t) = & \rho(t) + \frac{\Delta t}{\hbar} \left(-i[\hat{H}, \rho(t)] \right. \\ & + \sum_j^{\mathcal{Q}} \frac{\gamma}{2} \mathcal{L}(\rho(t), \hat{b}_j) \\ & + \sum_j^{\mathcal{Q}} \sum_{k=1,2} W_{jk} [\hat{a}_k \rho(t), \hat{b}_j^\dagger] + [\hat{b}_j, \rho(t) \hat{a}_k^\dagger] \\ & \left. + \sum_{k=1,2} \frac{\chi_k}{2} \mathcal{L}(\rho(t), \hat{a}_k) \right), \quad (\text{A2}) \end{aligned}$$

where we have used $\mathcal{L}(\rho, \hat{O}) \equiv 2\hat{O}\rho\hat{O}^\dagger - \hat{O}^\dagger\hat{O}\rho - \rho\hat{O}^\dagger\hat{O}$ and $\chi_k = \sum_j^{\mathcal{Q}} W_{jk}^2/\gamma$. In this formalism, γ denotes the energy decay of the network nodes, while χ_k is that of the input party k . The input-network coupling strength is characterised by W_{jk} .

Appendix B: Noise channels

Here we provide detailed expressions for the energy decay, dephasing, and depolarising channels. These channels are applied on the quantum network nodes, which are two-level quantum systems. See Ref. [87] for a review.

The energy decay channel models the decay of excitations, i.e., from excited state to ground state over time. It is denoted by the operator $\hat{D}_{\text{dcy}}(\Delta t)$, which is defined as follows:

$$\begin{aligned} \rho(t + \Delta t) = & \hat{D}_{\text{dcy}}(\Delta t)[\rho(t)] \quad (\text{B1}) \\ = & \sum_j^{\mathcal{Q}} \hat{K}_{j,1} \rho(t) \hat{K}_{j,1}^\dagger + \hat{K}_{j,2} \rho(t) \hat{K}_{j,2}^\dagger, \end{aligned}$$

where

$$\begin{aligned} \hat{K}_{j,1} = & \begin{bmatrix} 1 & 0 \\ 0 & \sqrt{1 - \frac{\gamma_{\text{dcy}}}{\hbar} \Delta t} \end{bmatrix}, \\ \hat{K}_{j,2} = & \begin{bmatrix} 0 & \sqrt{\frac{\gamma_{\text{dcy}}}{\hbar} \Delta t} \\ 0 & 0 \end{bmatrix}, \quad (\text{B2}) \end{aligned}$$

are operators applied on the j th node. For simplicity, we have assumed that the decay strength γ_{dcy} is the same for all the nodes.

Quantum states may lose their coherence, i.e., the decay of superposition (off-diagonal elements of $\rho(t)$). In this case, the dephasing operator $\hat{D}_{\text{dph}}(\Delta t)$ is defined as:

$$\begin{aligned} \rho(t + \Delta t) = & \hat{D}_{\text{dph}}(\Delta t)[\rho(t)] \quad (\text{B3}) \\ = & \sum_j^{\mathcal{Q}} \left(1 - \frac{\gamma_{\text{dph}}}{2\hbar} \Delta t \right) \rho(t) + \frac{\gamma_{\text{dph}}}{2\hbar} \Delta t \hat{\sigma}_j^z \rho(t) \hat{\sigma}_j^z, \end{aligned}$$

where the dephasing is in the $\hat{\sigma}^z$ basis. The strength of this channel is characterised by γ_{dph} , which is assumed uniform.

Last, experimental conditions can also result in depolarisation of the quantum state $\rho(t)$, i.e., mixing with white noise. This is modelled by $\hat{D}_{\text{dpl}}(\Delta t)$ defined as:

$$\begin{aligned} \rho(t + \Delta t) = & \hat{D}_{\text{dpl}}(\Delta t)[\rho(t)] \quad (\text{B4}) \\ = & \sum_j^{\mathcal{Q}} \left(1 - \frac{\gamma_{\text{dpl}}}{\hbar} \Delta t \right) \rho(t) \\ & + \sum_j^{\mathcal{Q}} \sum_{\nu=x,y,z} \frac{\gamma_{\text{dpl}}}{3\hbar} \Delta t \hat{\sigma}_j^\nu \rho(t) \hat{\sigma}_j^\nu, \end{aligned}$$

where γ_{dpl} indicates the strength.

We have used Pauli matrices with the subscript j denoting the application on the j th QN node:

$$\hat{\sigma}_j^x = \begin{bmatrix} 0 & 1 \\ 1 & 0 \end{bmatrix}, \quad \hat{\sigma}_j^y = \begin{bmatrix} 0 & -i \\ i & 0 \end{bmatrix}, \quad \hat{\sigma}_j^z = \begin{bmatrix} 1 & 0 \\ 0 & -1 \end{bmatrix}. \quad (\text{B5})$$

Appendix C: Training of output layer

Here we describe the training of the output layer, i.e., the coefficients $\boldsymbol{\alpha} \equiv (\alpha_0, \alpha_1, \alpha_2, \dots, \alpha_{\mathcal{Q}})^T$ in Eq. (7). Consider N_{train} number of training sets, each of which consists of a known random phase, labelled ϕ_i , and the resulting mean values from the QN ($\langle n_{1,i} \rangle, \langle n_{2,i} \rangle, \dots, \langle n_{\mathcal{Q},i} \rangle$) with a measurement error ξ , where the subscript denotes the i th training set. From the training sets, the coefficients $\boldsymbol{\alpha}$ are obtained as follows:

$$\boldsymbol{\alpha} = (\mathbf{X}^T \mathbf{X} + \lambda \mathbf{1})^{-1} \mathbf{X}^T \mathbf{Y}, \quad (\text{C1})$$

where

$$\mathbf{X} = \begin{bmatrix} 1 & \langle n_{1,1} \rangle & \langle n_{2,1} \rangle & \cdots & \langle n_{\mathcal{Q},1} \rangle \\ 1 & \langle n_{1,2} \rangle & \langle n_{2,2} \rangle & \cdots & \langle n_{\mathcal{Q},2} \rangle \\ \vdots & \vdots & \vdots & \ddots & \vdots \\ 1 & \langle n_{1,N_{\text{train}}} \rangle & \langle n_{2,N_{\text{train}}} \rangle & \cdots & \langle n_{\mathcal{Q},N_{\text{train}}} \rangle \end{bmatrix} \quad (\text{C2})$$

and

$$\mathbf{Y} = \frac{1}{2} \begin{bmatrix} 1 - \cos(N\phi_1) \\ 1 - \cos(N\phi_2) \\ \vdots \\ 1 - \cos(N\phi_{N_{\text{train}}}) \end{bmatrix}. \quad (\text{C3})$$

The constant value $\lambda > 0$ is known as the ridge parameter.

Once we obtain the coefficients $\boldsymbol{\alpha}$, we can calculate the output signal, given a set of mean values from experiments, via $I_{\text{est}} = \alpha_0 + \alpha_1 \langle n_1 \rangle + \alpha_2 \langle n_2 \rangle + \dots + \alpha_Q \langle n_Q \rangle$. Next, from the output signal one can retrieve the phase ϕ_{est} via

$$\phi_{\text{est}} = \begin{cases} 0, & I_{\text{est}} < 0 \\ \frac{1}{N} \arccos(1 - 2I_{\text{est}}), & I_{\text{est}} \in [0, 1] \\ \pi/N, & I_{\text{est}} > 1. \end{cases} \quad (\text{C4})$$

For testing, we consider N_{test} sets, each with a testing phase ϕ_l and the corresponding mean values $(\langle n_{1,l} \rangle, \langle n_{2,l} \rangle, \dots, \langle n_{Q,l} \rangle)$, taking into account the measurement error ξ . To quantify the phase estimation error, we use

$$\Delta \bar{\phi}_N = \sqrt{\sum_l^{N_{\text{test}}} \frac{(\phi_{\text{est},l} - \phi_l)^2}{N_{\text{test}}(N_{\text{test}} - 1)}}, \quad (\text{C5})$$

where $\phi_{\text{est},l}$ is calculated as in Eq. (C4) and the subscript N indicates the use of N -NOON state as a resource.

We show the role of the ridge parameter λ by considering the exemplary task presented in Fig. 3(c) where $\xi = 10^{-3}$. In this case, we used 10 training sets and 100 testing sets. Fig. 9(a) demonstrates the testing error against the ridge parameter λ . It is clear that the case where $\lambda \rightarrow 0$ (linear regression limit) leads to overfitting of the training data, i.e., including the measurement error, and thus overlooking the real behaviour. On the other hand, higher value of λ leads to underfitting. The tradeoff results in a minimum error, at λ_{min} . The phase estimation errors reported in this paper follow this minimum error.

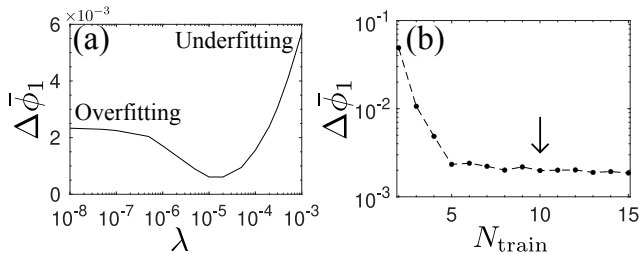


FIG. 9. Phase estimation error vs ridge parameter (a) and number of training sets (b). The arrow indicates the chosen N_{train} in this paper.

The number of training sets is another factor affecting the precision. To illustrate this, we plot in Fig. 9(b) the phase estimation error against the number of training

sets N_{train} . We have used a QN with size 4, $\xi = 10^{-3}$, and $N_{\text{test}} = 100$. Each point is averaged over 50 realizations of the network parameters. It can be seen that $\Delta \bar{\phi}_1$ decreases with N_{train} . We have chosen $N_{\text{train}} = 10$ throughout this paper.

Appendix D: Standard deviation of the mean at highest output slope

For any constant phase ϕ , one quantifies the phase estimation error with SDM $\Delta \phi_N$. Here we demonstrate the advantage of our platform in the training step. In particular, we consider a “shifted” ideal output signal:

$$I_{\text{ideal}} = \frac{1}{2} (1 - \cos(N(\phi + \theta))). \quad (\text{D1})$$

The phase shift θ is chosen such that the SDM of the phase $\Delta \phi_N$ is minimum. This corresponds to the phase ϕ situated at the highest slope of the output signal of Eq. (D1).

To illustrate this, we plotted the estimated output signal for both $\theta = 0$ and $\pi/4$ in Fig. 10 panels (a) and (b), respectively. We used the same training set ($N_{\text{train}} = 10$) and testing set ($N_{\text{test}} = 100$) in both panels. Also, we used $Q = 4$ with $\tau = 8/\Omega$ and $\xi = 10^{-2}$. The highest output slope shifts from $\phi = \pi/2$ in (a) to $\pi/4$ in (b). Phase estimation in the range indicated by the green dashed boxes are plotted in panels (c) and (d). It can be seen that the minimum error is located at the highest output slope. In the data processing, one simply varies the phase shift θ until $\Delta \phi_N$ is minimised.

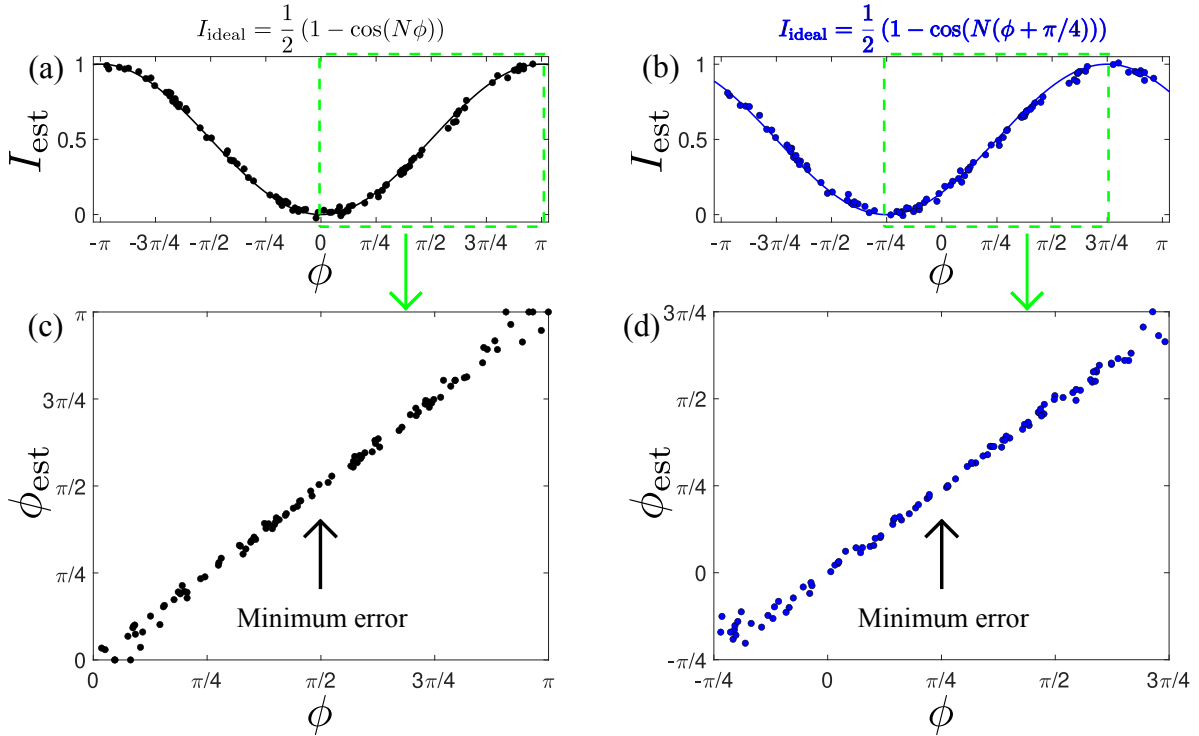


FIG. 10. Minimising the SDM with shifted output signal. The same training set and testing set are used for different target output $\theta = 0$ (a) and $\pi/4$ (b). The corresponding phase estimation tasks in the range indicated by the green dashed boxes are plotted in (c) and (d), respectively. The minimum error shifts from $\theta = 0$ (a) to $\pi/4$ (b).

-
- [1] V. Giovannetti, S. Lloyd, and L. Maccone, Quantum-enhanced measurements: beating the standard quantum limit, *Science* **306**, 1330 (2004).
- [2] T. Nagata, R. Okamoto, J. L. O'Brien, K. Sasaki, and S. Takeuchi, Beating the standard quantum limit with four-entangled photons, *Science* **316**, 726 (2007).
- [3] B. L. Higgins, D. W. Berry, S. D. Bartlett, H. M. Wiseman, and G. J. Pryde, Entanglement-free Heisenberg-limited phase estimation, *Nature* **450**, 393 (2007).
- [4] S. Slussarenko *et al.*, Unconditional violation of the shot-noise limit in photonic quantum metrology, *Nat. Photonics* **11**, 700 (2017).
- [5] S. Daryanoosh, S. Slussarenko, D. W. Berry, H. M. Wiseman, and G. J. Pryde, Experimental optical phase measurement approaching the exact Heisenberg limit, *Nat. Commun.* **9**, 4606 (2018).
- [6] C. Gross, T. Zibold, E. Nicklas, J. Esteve, and M. K. Oberthaler, Nonlinear atom interferometer surpasses classical precision limit, *Nature* **464**, 1165 (2010).
- [7] B. Lücke *et al.*, Twin matter waves for interferometry beyond the classical limit, *Science* **334**, 773 (2011).
- [8] K. C. McCormick, J. Keller, S. C. Burd, D. J. Wineland, A. C. Wilson, and D. Leibfried, Quantum-enhanced sensing of a single-ion mechanical oscillator, *Nature* **572**, 86 (2019).
- [9] J. A. Jones *et al.*, Magnetic field sensing beyond the standard quantum limit using 10-spin NOON states, *Science* **324**, 1166 (2009).
- [10] M. Napolitano, M. Koschorreck, B. Dubost, N. Behbood, R. J. Sewell, and M. W. Mitchell, Interaction-based quantum metrology showing scaling beyond the Heisenberg limit, *Nature* **471**, 486 (2011).
- [11] J. Kong, R. Jiménez-Martínez, C. Troullinou, V. G. Lucivero, G. Tóth, and M. W. Mitchell, Measurement-induced, spatially-extended entanglement in a hot, strongly-interacting atomic system, *Nat. Commun.* **11**, 2415 (2020).
- [12] A. Facon, E.-K. Dietsche, D. Grosso, S. Haroche, J.-M. Raimond, M. Brune, and S. Gleyzes, A sensitive electrometer based on a Rydberg atom in a Schrödinger-cat state, *Nature* **535**, 262 (2016).
- [13] H. Yu *et al.*, Quantum correlations between light and the kilogram-mass mirrors of LIGO, *Nature* **583**, 43 (2020).
- [14] P. Walther *et al.*, De Broglie wavelength of a non-local four-photon state, *Nature* **429**, 158 (2004).
- [15] M. W. Mitchell, J. S. Lundeen, and A. M. Steinberg, Super-resolving phase measurements with a multiphoton entangled state, *Nature* **429**, 161 (2004).
- [16] K. J. Resch *et al.*, Time-Reversal and Super-Resolving Phase Measurements, *Phys. Rev. Lett.* **98**, 223601 (2007).
- [17] S. Webb, Deep learning for biology, *Nature* **554** (2018).
- [18] D. T. Jones, Setting the standards for machine learning in biology, *Nat. Rev. Mol. Cell Biol.* **20**, 659 (2019).
- [19] E. J. Topol, High-performance medicine: the convergence of human and artificial intelligence, *Nat. Med.* **25**, 44

- (2019).
- [20] A. Y. Hannun, Cardiologist-level arrhythmia detection and classification in ambulatory electrocardiograms using a deep neural network, *Nat. Med.* **25**, 65 (2019).
- [21] A. Nagy and V. Savona, Variational Quantum Monte Carlo Method with a Neural-Network Ansatz for Open Quantum Systems, *Phys. Rev. Lett.* **122**, 250501 (2019).
- [22] M. J. Hartmann and G. Carleo, Neural-Network Approach to Dissipative Quantum Many-Body Dynamics, *Phys. Rev. Lett.* **122**, 250502 (2019).
- [23] F. Vicentini, A. Biella, N. Regnault, and C. Ciuti, Variational Neural-Network Ansatz for Steady States in Open Quantum Systems, *Phys. Rev. Lett.* **122**, 250503 (2019).
- [24] P. Mehta *et al.*, A high-bias, low-variance introduction to machine learning for physicists, *Phys. Rep.* **810**, 1 (2019).
- [25] G. Montavon, G. Orr, and K.-R. Müller, *Neural networks: tricks of the trade* (Springer, 2012).
- [26] G. Wetzstein, A. Ozcan, S. Gigan, S. Fan, D. Englund, M. Soljačić, C. Denz, D. A. Miller, and D. Psaltis, Inference in artificial intelligence with deep optics and photonics, *Nature* **588**, 39 (2020).
- [27] K. Vandoorne, P. Mechet, T. Van Vaerenbergh, M. Fiers, G. Morthier, D. Verstraeten, B. Schrauwen, J. Dambre, and P. Bienstman, Experimental demonstration of reservoir computing on a silicon photonics chip, *Nat. Commun.* **5**, 3541 (2014).
- [28] R. M. Nguimdo, G. Verschaffelt, J. Danckaert, and G. Van der Sande, Simultaneous computation of two independent tasks using reservoir computing based on a single photonic nonlinear node with optical feedback, *IEEE Trans. Neural Netw. Learn. Syst.* **26**, 3301 (2015).
- [29] G. Van der Sande, D. Brunner, and M. C. Soriano, Advances in photonic reservoir computing, *Nanophotonics* **6**, 561 (2017).
- [30] D. Brunner, M. C. Soriano, and G. Van der Sande, Photonic reservoir computing, *De Gruyter* **8**, 19 (2019).
- [31] G. Tanaka *et al.*, Recent advances in physical reservoir computing: A review, *Neural Netw.* **115**, 100 (2019).
- [32] D. Ballarini *et al.*, Polaritonic neuromorphic computing outperforms linear classifiers, *Nano Lett.* **20**, 3506 (2020).
- [33] M. Rafayelyan, J. Dong, Y. Tan, F. Krzakala, and S. Gigan, Large-scale optical reservoir computing for spatiotemporal chaotic systems prediction, *Phys. Rev. X* **10**, 041037 (2020).
- [34] A. P. Dash *et al.*, Explicit demonstration of initial state construction in artificial neural networks using NetKet and IBM Q experience platform, *Quantum Inf. Process.* **19**, 21 (2020).
- [35] J. Shi *et al.*, An Approach to cryptography Based on continuous-Variable Quantum neural network, *Sci. Rep.* **10**, 2107 (2020).
- [36] D. Przychyna, S. Pecqueur, D. Vuillaume, and K. Szacilowski, Reservoir computing for sensing: an experimental approach, arXiv:2001.04342 (2020).
- [37] K. Fujii and K. Nakajima, Harnessing disordered-ensemble quantum dynamics for machine learning, *Phys. Rev. Appl.* **8**, 024030 (2017).
- [38] L. C. G. Govia, G. J. Ribeill, G. E. Rowlands, H. K. Krovi, and T. A. Ohki, Quantum reservoir computing with a single nonlinear oscillator, *Phys. Rev. Res.* **3**, 013077 (2021).
- [39] W. D. Kalfus, G. J. Ribeill, G. E. Rowlands, H. K. Krovi, T. A. Ohki, and L. C. G. Govia, Neuromorphic computing with a single qudit, arXiv:2101.11729 (2021).
- [40] H. Xu, T. Krisnanda, W. Verstraelen, T. C. H. Liew, and S. Ghosh, Superpolynomial quantum enhancement in polaritonic neuromorphic computing, *Phys. Rev. B* **103**, 195302 (2021).
- [41] S. Ghosh, A. Opala, M. Matuszewski, T. Paterek, and T. C. H. Liew, Quantum reservoir processing, *npj Quantum Inf.* **5**, 35 (2019).
- [42] S. Ghosh, A. Opala, M. Matuszewski, T. Paterek, and T. C. H. Liew, Reconstructing quantum states with quantum reservoir networks, *IEEE Trans. Neural Netw. Learn. Syst.* **32**, 3148 (2020).
- [43] S. Ghosh, T. Paterek, and T. C. H. Liew, Quantum Neuromorphic Platform for Quantum State Preparation, *Phys. Rev. Lett.* **123**, 260404 (2019).
- [44] T. Krisnanda, S. Ghosh, T. Paterek, and T. C. H. Liew, Creating and concentrating quantum resource states in noisy environments using a quantum neural network, *Neural Netw.* **136**, 141 (2021).
- [45] S. Ghosh, T. Krisnanda, T. Paterek, and T. C. H. Liew, Realising and compressing quantum circuits with quantum reservoir computing, *Commun. Phys.* **4**, 105 (2021).
- [46] D. Marković and J. Grollier, Quantum neuromorphic computing, *Appl. Phys. Lett.* **117**, 150501 (2020).
- [47] S. Ghosh, K. Nakajima, T. Krisnanda, K. Fujii, and T. C. H. Liew, Quantum Neuromorphic Computing with Reservoir Computing Networks, *Adv. Quantum Technol.*, 2100053.
- [48] A. P. Alivisatos, Semiconductor clusters, nanocrystals, and quantum dots, *Science* **271**, 933 (1996).
- [49] D. Bimberg, M. Grundmann, and N. N. Ledentsov, *Quantum dot heterostructures* (John Wiley & Sons, 1999).
- [50] T. Esslinger, Fermi-Hubbard physics with atoms in an optical lattice, *Annu. Rev. Condens. Matter Phys.* **1**, 129 (2010).
- [51] W. Hofstetter and T. Qin, Quantum simulation of strongly correlated condensed matter systems, *J. Phys. B* **51**, 082001 (2018).
- [52] L. Tarruell and L. Sanchez-Palencia, Quantum simulation of the Hubbard model with ultracold fermions in optical lattices, *C. R. Phys.* **19**, 365 (2018).
- [53] D. E. Chang, V. Vuletić, and M. D. Lukin, Quantum nonlinear optics—photon by photon, *Nat. Photonics* **8**, 685 (2014).
- [54] A. V. Poshakinskiy, J. Zhong, Y. Ke, N. A. Olekhno, C. Lee, Y. S. Kivshar, and A. N. Poddubny, Quantum hall phases emerging from atom–photon interactions, *npj Quantum Inf.* **7**, 34 (2021).
- [55] A. Browaeys and T. Lahaye, Many-body physics with individually controlled Rydberg atoms, *Nat. Phys.* **16**, 132 (2020).
- [56] I. Carusotto *et al.*, Fermionized Photons in an Array of Driven Dissipative Nonlinear Cavities, *Phys. Rev. Lett.* **103**, 033601 (2009).
- [57] C.-E. Bardyn and A. İmamoĖşlu, Majorana-like Modes of Light in a One-Dimensional Array of Nonlinear Cavities, *Phys. Rev. Lett.* **109**, 253606 (2012).
- [58] C. Vaneph *et al.*, Observation of the Unconventional Photon Blockade in the Microwave Domain, *Phys. Rev. Lett.* **121**, 043602 (2018).
- [59] J. Moughames, X. Porte, M. Thiel, G. Ulliac, L. Larger, M. Jacquot, M. Kadic, and D. Brunner, Three-dimensional waveguide interconnects for scalable integra-

- tion of photonic neural networks, *Optica* **7**, 640 (2020).
- [60] D. G. Angelakis, *Quantum Simulations with Photons and Polaritons* (Springer, 2017).
- [61] A. Delteil *et al.*, Towards polariton blockade of confined exciton-polaritons, *Nat. Mater.* **18**, 219 (2019).
- [62] R. P. A. Emmanuele *et al.*, Highly nonlinear trion-polaritons in a monolayer semiconductor, *Nat. Commun.* **11**, 3589 (2020).
- [63] O. Kyriienko, D. N. Krizhanovskii, and I. A. Shelykh, Nonlinear Quantum Optics with Trion Polaritons in 2D Monolayers: Conventional and Unconventional Photon Blockade, *Phys. Rev. Lett.* **125**, 197402 (2020).
- [64] S. Haroche, M. Brune, and J. Raimond, From cavity to circuit quantum electrodynamics, *Nat. Phys.* **16**, 243 (2020).
- [65] A. Blais, S. M. Girvin, and W. D. Oliver, Quantum information processing and quantum optics with circuit quantum electrodynamics, *Nat. Phys.* **16**, 247 (2020).
- [66] A. A. Clerk, K. W. Lehnert, P. Bertet, J. R. Petta, and Y. Nakamura, Hybrid quantum systems with circuit quantum electrodynamics, *Nat. Phys.* **16**, 257 (2020).
- [67] I. Carusotto, A. A. Houck, A. J. Kollár, P. Roushan, D. I. Schuster, and J. Simon, Photonic materials in circuit quantum electrodynamics, *Nat. Phys.* **16**, 268 (2020).
- [68] S. Leedumrongwatthanakun, L. Innocenti, H. Defienne, T. Juffmann, A. Ferraro, M. Paternostro, and S. Gigan, Programmable linear quantum networks with a multi-mode fibre, *Nat. Photonics* **14**, 139 (2020).
- [69] I. Afek, O. Ambar, and Y. Silberberg, High-NOON states by mixing quantum and classical light, *Science* **328**, 879 (2010).
- [70] R. Horodecki, P. Horodecki, M. Horodecki, and K. Horodecki, Quantum entanglement, *Rev. Mod. Phys.* **81**, 865 (2009).
- [71] G. Vidal and R. F. Werner, Computable measure of entanglement, *Phys. Rev. A* **65**, 032314 (2002).
- [72] L. Henderson and V. Vedral, Classical, quantum and total correlations, *J. Phys. A* **34**, 6899 (2001).
- [73] H. Ollivier and W. H. Zurek, Quantum Discord: A Measure of the Quantumness of Correlations, *Phys. Rev. Lett.* **88**, 017901 (2001).
- [74] A. Streltsov, H. Kampermann, and D. Bruß, Quantum Cost for Sending Entanglement, *Phys. Rev. Lett.* **108**, 250501 (2012).
- [75] T. K. Chuan, J. Maillard, K. Modi, T. Paterek, M. Paternostro, and M. Piani, Quantum Discord Bounds the Amount of Distributed Entanglement, *Phys. Rev. Lett.* **109**, 070501 (2012).
- [76] T. Krisnanda, M. Zuppardo, M. Paternostro, and T. Paterek, Revealing Nonclassicality of Inaccessible Objects, *Phys. Rev. Lett.* **119**, 120402 (2017).
- [77] T. Krisnanda, Distribution of quantum entanglement: Principles and applications, arXiv:2003.08657 (2020).
- [78] K. Modi, H. Cable, M. Williamson, and V. Vedral, Quantum correlations in mixed-state metrology, *Phys. Rev. X* **1**, 021022 (2011).
- [79] T. Baumgratz, M. Cramer, and M. B. Plenio, Quantifying Coherence, *Phys. Rev. Lett.* **113**, 140401 (2014).
- [80] S. Boixo, S. T. Flammia, C. M. Caves, and J. M. Geremia, Generalized Limits for Single-Parameter Quantum Estimation, *Phys. Rev. Lett.* **98**, 090401 (2007).
- [81] S. Choi and B. Sundaram, Bose-Einstein condensate as a nonlinear Ramsey interferometer operating beyond the Heisenberg limit, *Phys. Rev. A* **77**, 053613 (2008).
- [82] S. M. Roy and S. L. Braunstein, Exponentially Enhanced Quantum Metrology, *Phys. Rev. Lett.* **100**, 220501 (2008).
- [83] C. W. Gardiner, Driving a quantum system with the output field from another driven quantum system, *Phys. Rev. Lett.* **70**, 2269 (1993).
- [84] H. J. Carmichael, Quantum trajectory theory for cascaded open systems, *Phys. Rev. Lett.* **70**, 2273 (1993).
- [85] Y. M. Zhang, X. W. Li, W. Yang, and G. R. Jin, Quantum Fisher information of entangled coherent states in the presence of photon loss, *Phys. Rev. A* **88**, 043832 (2013).
- [86] J. Liu, X. Jing, and X. Wang, Phase-matching condition for enhancement of phase sensitivity in quantum metrology, *Phys. Rev. A* **88**, 042316 (2013).
- [87] M. A. Nielsen and I. L. Chuang, *Quantum computation and quantum information* (Cambridge University Press, 2010).